



## 3D Catheter Shape Reconstruction Using Electromagnetic and Image Sensors

Phuong Toan Tran<sup>\*,¶</sup>, Ping-Lin Chang<sup>†</sup>, Herbert De Praetere<sup>‡</sup>,  
Julies Maes<sup>§</sup>, Dominiek Reynaerts<sup>\*</sup>, Jos Vander Sloten<sup>\*</sup>, Danail Stoyanov<sup>†</sup>,  
Emmanuel Vander Poorten<sup>\*</sup>

<sup>\*</sup>Department of Mechanical Engineering, KU Leuven, BE-3001 Leuven, Belgium

<sup>†</sup>Centre for Medical Image Computing, University College London, NW1 3EE London, United Kingdom

<sup>‡</sup>Department of Experimental Cardiac Surgery, University Hospital Leuven, BE-3000 Leuven, Belgium

<sup>§</sup>Materialise NV, BE-3001 Leuven, Belgium

In current practice, fluoroscopy remains the gold standard for guiding surgeons during endovascular catheterization. The poor visibility of anatomical structures and the absence of depth information make accurate catheter localization and manipulation a difficult task. Overexposure to radiation and use of risk-prone contrast agent also compromise surgeons' and patients' health. Alternative approaches using embedded electromagnetic (EM) sensors have been developed to overcome the limitations of fluoroscopy-based interventions. As only a finite number of sensors can be integrated within a catheter, methods that rely on such sensors require the use of interpolation schemes to recover the catheter shape. Since EM sensors are sensitive to external interferences, the outcome is not robust. This paper introduces a probabilistic framework that improves the catheter localization and reduces the dependency on fluoroscopy and contrast agents. Within this framework, the dense 2D information extracted from fluoroscopic images is combined with the discrete pose information of EM sensors to provide a reliable reconstruction of the full three-dimensional catheter shape. Validation in a physics-based simulation environment and in a real-world experimental setup provides promising results and indicates that the proposed framework allows reconstructing the 3D catheter shape with a median root-mean-square error of 3.7 mm with an interquartile range of 0.3 mm.

**Keywords:** Shape reconstruction; tracking; fluoroscopy; electromagnetic; probabilistic framework; catheter.

JMRR

### 1. Introduction

Minimally invasive surgery provides many benefits for the patient but generally comes with a high procedural complexity [1]. This is particularly the case for endovascular catheterization where the limited field of view and restricted access to the patient's anatomy requires

external imaging to guide the surgeon during the procedure. For example, in transcatheter aortic valve implantation (TAVI), fluoroscopy is typically used for localizing the catheter while navigating to the natural aortic valve and further for guiding the delivery and placement of the artificial valve [2]. The procedure is challenging because fluoroscopic images do not convey the full 3D spatial relationship between the catheter and its surrounding environment. The heart and blood vessels are difficult to visualize, and contrast agent driven road mapping — with its associated risks — is often required. Enhanced visual feedback with a reduced dependency on damaging imaging modalities would therefore be beneficial for both patients and surgeons. Combined with 3D preoperative data, a full 3D catheter shape reconstructed from sensory data could help the

Received 31 March 2016; Revised 20 June 2016; Accepted 14 October 2016; Published 21 March 2017. Published in JMRR Special Issue on CRAS 2015. Guest Editors: Leonardo Mattos, Paolo Fiorini, Emmanuel Benjamin Vander Poorten and Benoît Herman.

Email Address: ¶[phuongtoan.tran@kuleuven.be](mailto:phuongtoan.tran@kuleuven.be)

NOTICE: Prior to using any material contained in this paper, the users are advised to consult with the individual paper author(s) regarding the material contained in this paper, including but not limited to, their specific design(s) and recommendation(s).

surgeon to avoid risk-prone areas by providing a better understanding of the catheter's spatial configuration within the patient's anatomy. Such technology could also support real-time skill assessment systems [3], as well as (semi-)autonomous control schemes for navigation of robotic catheters [4, 5].

In the past, different approaches and sensing modalities have been proposed for catheter tracking and localization. Several strategies are based on fluoroscopic images [6, 7] but can only provide 2D information unless bi-planar imaging is used [8]. Other approaches make use of sensors that are embedded within the catheter's body to provide proprioceptive sensing capabilities [9–11]. In particular, embedded electromagnetic (EM) sensors have been used as pose sensing modality for various minimally invasive procedures [9]. However, EM sensors only provide discrete pose information along the catheter, and only a limited number of them can be integrated into catheters. Such approaches thus necessitate the adoption of interpolation schemes to estimate the entire catheter shape. Furthermore, a method that solely relies on EM tracking shows limited robustness as the measurement accuracy is affected by the presence of ferromagnetic materials and external EM fields in the operating room. In principle, dedicated shielding or calibration procedures combined with active compensation and/or filtering [9, 12] can account for EM disturbances. In reality, these methods are often found impractical in the operating room. Another approach consists in fusing the EM measurements with other sensing information and/or predictive models [13–15] to compensate for these interferences. These probabilistic approaches however either rely on a well-defined model or focus on improving only the pose of the EM sensors, especially for the one located at the catheter tip.

Other approaches that do not rely on EM sensing have shown promising results. Vandini *et al.* uses fluoroscopic information to improve the 3D shape of concentric tube robots that is estimated from a kinematic model specific to concentric tube robots [16]. Shape sensing based on optical fibers is attractive, but suffers from hardware integration issues and spectral distortion for strong bendings [17–20].

In this paper, we introduce a probabilistic framework that combines EM measurements and fluoroscopic images to provide a reliable estimate of the full 3D catheter shape. This framework extends Chang *et al.*'s work about catheter tracking in fluoroscopic images [21] by incorporating EM data to recover a 3D shape. The proposed approach still relies on fluoroscopy, as it will likely maintain its dominant role as imaging modality for endovascular surgery. However, the proposed method could contribute to reduce the dependency on fluoroscopy by only using it in risk-prone areas where an accurate catheter shape reconstruction is needed, relying solely on EM sensing for less critical areas. To validate

our approach and separate the reconstruction error from other sources of error, the proposed framework was first evaluated in a physics-based simulation environment that provides ground-truth catheter shapes during virtual catheterization and generates the corresponding synthetic fluoroscopic images and EM sensor data. The framework was then evaluated in a real-world experimental setup with real sensor data.

The paper is organized as follows. Section 2 outlines the proposed probabilistic framework. Section 3 describes the experimental setups that were used to evaluate the framework and presents the results. Finally, Sec. 4 concludes the paper and sketches some directions for future developments.

## 2. Probabilistic Framework

Within the proposed framework, the catheter is modeled as a 3D B-spline tube. It embeds several EM sensors and generates a 2D projection of its shape in the fluoroscopic image. The 3D and 2D catheter shapes are related through a projection function derived from a conventional pinhole camera model. The contour of the 2D projected catheter shape delimits the foreground and background regions of the fluoroscopic image. The former is associated with the pixels that are within the 2D catheter shape, while the latter represents the remaining pixels. This is illustrated in Fig. 1. The following notations are used throughout the paper:

- $\zeta$  3D B-spline tube model representing the catheter.
- $b$  Cubic B-spline representing the catheter centerline.
- $C$   $\{C_1, \dots, C_n\}$  3D control points of  $b$ .
- $K$   $\{K_1, \dots, K_n\}$  3D knot points of  $b$ .
- $D$   $\{D_1, \dots, D_{n_s}\} = \{\{p_1, t_1\}, \dots, \{p_{n_s}, t_{n_s}\}\}$  EM measurements in the 3D world space, with  $\{p_i, t_i\}$  describing the 5-DOFs pose of the sensor:  $p_i$  is the sensor 3D position and  $t_i$  is the unit tangent vector to the curve at  $p_i$ .
- $\pi$  Projection function projecting a 3D point from the world space to the 2D image.
- $\tau$  2D closed contour as the projected contour of  $\zeta$ .
- $M$   $\{M_f, M_b\}$  foreground and background models of the 2D image.
- $\Omega$   $\{\Omega_f, \Omega_b\} = \{\{x_1, y_1\}, \dots, \{x_{|\Omega|}, y_{|\Omega|}\}\}$  image domain.
- $x$   $\{x_1, \dots, x_{|\Omega|}\}$  pixel locations in the 2D image.
- $y$   $\{y_1, \dots, y_{|\Omega|}\}$  pixel measurements in the 2D image (gray intensity and Frangi filtering magnitude).

The graphical model in Fig. 1 shows the dependency between these elements.

The core of the proposed framework consists in a joint optimization of the 3D B-spline tube model in the fluoroscopic image plane and in 3D Cartesian space. Fluoroscopic data allows tracking of the catheter within the fluoroscopic image plane, while EM sensors are used

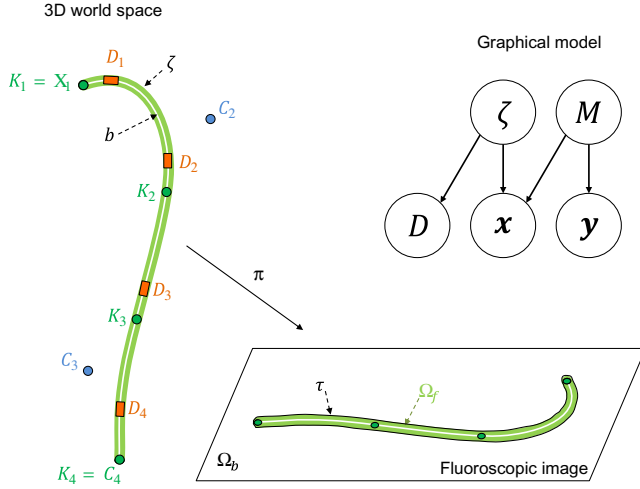


**Fig. 1.** The catheter is modeled as a 3D B-spline tube with EM sensors  $D_i$  (orange rectangles), control points  $C_i$  (blue circles), knot points  $K_i$  (green circles), the cubic B-spline  $b$  (white curve), and the 3D tube model  $\zeta$  (green tube). The 3D shape is projected (with a projection function  $\pi$ ) on the 2D fluoroscopic image to define a contour  $\tau$  which delimits the foreground  $\Omega_f$  and background  $\Omega_b$  regions. The graphical model shows the dependency between the elements involved in the overall reconstruction problem: the 3D B-spline tube model  $\zeta$ , the EM sensor data  $D$ , the foreground and background models  $M = \{M_f, M_b\}$ , the pixel locations  $\mathbf{x}$  and the image measurements  $\mathbf{y}$ .

to recover the depth information. The following sections describe the proposed framework in greater details.

## 2.1. B-spline tube model

The standard basis function representation of a B-spline curve of degree  $k - 1$  is given by:

$$\mathbf{b}(t) = \sum_{i=1}^n \mathbf{C}_i B_{i,k}(t), \quad (1)$$

where  $\mathbf{C}_i \in \mathbb{R}^N$  are the control points and  $B_{i,k}(t)$  are basis functions which can be derived by the De Boor-Cox recursive formula [22]. In this paper, the focus is on the particular case of three-dimensional cubic open B-splines with degree 3 ( $N = 3$  and  $k = 4$ ) which are  $\mathbb{C}^2$  continuously differentiable functions.

Unlike conventional fitting schemes that optimize the B-spline control points, the proposed framework uses a knot-driven representation to fit a clamped B-spline to the measurements. This provides better local control, especially for tracking the catheter in the fluoroscopic image [21]. The knot point representation of a B-spline can be derived from the local definition of the B-spline. For a cubic B-spline, four control points  $[\mathbf{C}_{i-1}, \mathbf{C}_i, \mathbf{C}_{i+1}, \mathbf{C}_{i+2}]$  influence the local value of the spline curve. Using the matrix representation of the De Boor-Cox formula,

the local cubic B-spline can be defined as a linear combination of the local control points [23]:

$$\mathbf{b}_i(t) = \frac{1}{6} \begin{bmatrix} t^3 & t^2 & t & 1 \end{bmatrix} \begin{bmatrix} -1 & 3 & -3 & 1 \\ 3 & -6 & 3 & 0 \\ -3 & 0 & 3 & 0 \\ 1 & 4 & 1 & 0 \end{bmatrix} \begin{bmatrix} \mathbf{C}_{i-1} \\ \mathbf{C}_i \\ \mathbf{C}_{i+1} \\ \mathbf{C}_{i+2} \end{bmatrix}. \quad (2)$$

For point interpolation, a clamped cubic B-spline has  $\mathbf{C}_{j \in -2, \dots, n+3}$  and, at the boundaries,  $\mathbf{C}_1 = \mathbf{C}_{j < 1}$  and  $\mathbf{C}_n = \mathbf{C}_{j > n}$ . The sampling parameter  $t \in [0, 1]$  is uniformly distributed for point interpolation. The knot points are then defined at  $t = 0$ :

$$\mathbf{K}_i = \mathbf{b}_i(0) = \frac{1}{6} \mathbf{C}_{i-1} + \frac{2}{3} \mathbf{C}_i + \frac{1}{6} \mathbf{C}_{i+1}. \quad (3)$$

Finally, given a set of knot points  $\mathbf{K}_i$ , the control points for a clamped cubic B-spline can be found by

$$\begin{bmatrix} \mathbf{C}_1 \\ \vdots \\ \mathbf{C}_n \end{bmatrix} = \begin{bmatrix} 1 & & & \dots & & 0 \\ \frac{1}{6} & \frac{2}{3} & \frac{1}{6} & & & \\ & \ddots & \ddots & \ddots & & \vdots \\ & & \frac{1}{6} & \frac{2}{3} & \frac{1}{6} & \\ \vdots & & & \ddots & \ddots & \ddots \\ 0 & & & & \frac{1}{6} & \frac{2}{3} & \frac{1}{6} \\ & & & & & & 1 \end{bmatrix}^{-1} \begin{bmatrix} \mathbf{K}_1 \\ \vdots \\ \mathbf{K}_n \end{bmatrix} \quad (4)$$

with  $n \geq 4$ . Note that for the inverse transformation the number of control points and knot points are equivalent, and at the boundary  $\mathbf{K}_1 = \mathbf{C}_1$  and  $\mathbf{K}_n = \mathbf{C}_n$  due to the clamp.

A tube model  $\zeta$  can thus be defined by a set of knot points followed by Eq. (4) to obtain the corresponding control points and Eq. (2) to interpolate the B-spline. As the diameter of the tube can be estimated from the real catheter, the overall optimization scheme needs to only consider the knot points. An example of a tube model fitted by four knot points is shown in Fig. 1.

## 2.2. Posterior for shape reconstruction

Reconstruction of the 3D catheter shape is achieved by optimizing the posterior  $P(\zeta|D, \Omega)$ , which is defined as the probability of the tube model  $\zeta$  given the EM data  $D$  and all pixel data  $\Omega$ . The graphical model shown in Fig. 1 is used to derive this posterior. The following joint probability is given by the graphical model:

$$P(D, \mathbf{x}, \mathbf{y}, \zeta, M) = P(D|\zeta)P(\mathbf{x}|\zeta, M)P(\mathbf{y}|M)P(\zeta)P(M). \quad (5)$$

Assuming that  $\mathbf{x}$ ,  $\mathbf{y}$  and  $D$  are independent from each other (as shown by the graphical model in Fig. 1), we divide Eq. (5) successively by  $P(\mathbf{y})$ ,  $P(\mathbf{x})$  and  $P(D)$ , and obtain:

$$\begin{aligned} P(\zeta, M|\mathbf{x}, \mathbf{y}, D) &= \frac{1}{P(\mathbf{x})} P(\zeta|D) P(\mathbf{x}|\zeta, M) P(M|\mathbf{y}) \\ &= \frac{1}{P(\mathbf{x})} P(\zeta|D) \sum_j P(\mathbf{x}|\zeta, M_j) P(M_j|\mathbf{y}). \end{aligned} \quad (6)$$

Using  $M$  as a hidden variable and assuming the independence between  $M$  and  $\zeta$  and between  $\mathbf{x}$  and  $\mathbf{y}$ , we can write

$$\begin{aligned} P(\mathbf{x}|\zeta, \mathbf{y}) &= \sum_j P(\mathbf{x}, M_j|\zeta, \mathbf{y}) \\ &= \sum_j P(\mathbf{x}|\zeta, M_j) P(M_j|\mathbf{y}) \end{aligned} \quad (7)$$

and marginalize out  $M$  in Eq. (6):

$$P(\zeta|\mathbf{x}, \mathbf{y}, D) = \frac{1}{P(\mathbf{x})} P(\mathbf{x}|\zeta, \mathbf{y}) P(\zeta|D). \quad (8)$$

Finally, we consider  $P(\mathbf{x})$  constant with respect to  $\zeta$ , which yields

$$P(\zeta|\Omega, D) = P(\zeta|\mathbf{x}, \mathbf{y}, D) \propto P(\mathbf{x}|\zeta, \mathbf{y}) P(\zeta|D). \quad (9)$$

Maximizing the posterior  $P(\zeta|\Omega, D)$  is a maximum *a posteriori* (MAP) problem which comes down to maximize both the likelihood  $P(\mathbf{x}|\zeta, \mathbf{y})$  and the prior  $P(\zeta|D)$ . In practice, we perform a maximum likelihood estimation (MLE) with respect to  $\zeta$  in the 2D fluoroscopic image and treat the prior as another MAP problem for reconstructing  $\zeta$  in 3D. The MLE and MAP problems are alternatively performed until convergence of  $P(\zeta|\Omega, D)$ .

### 2.2.1. MAP for 3D reconstruction

The prior  $P(\zeta|D)$  in Eq. (9) can also be regarded as a posterior of  $\zeta$  given the EM data  $D$ . Assuming the noise model  $P(D)$  constant with respect to  $\zeta$ , we aim to maximize

$$P(\zeta|D) \propto P(D|\zeta) P(\zeta) \quad (10)$$

to reconstruct the 3D catheter shape solely based on EM data. The likelihood  $P(D|\zeta)$  describes how likely the current EM measurements are to be explained by the B-spline tube model  $\zeta$ , while the prior  $P(\zeta)$  accounts for any prior knowledge concerning the catheter.

Given  $n_s$  EM data  $\{D_1, \dots, D_{n_s}\}$  (with  $D_1$  the EM data the closest to the catheter tip), the likelihood in Eq. (10) can be expressed as:

$$\begin{aligned} P(D|\zeta) &= P(D_1 \dots D_{n_s}|\zeta) \\ &= P(D_{n_s}|\zeta, D_1, \dots, D_{n_s-1}) \dots P(D_2|\zeta, D_1) P(D_1|\zeta). \end{aligned} \quad (11)$$

In Eq. (11), the probability distribution associated to the measurement  $D_i$  models the deviation of the estimated tube model  $\zeta$  with respect to the EM sensor pose  $\{\mathbf{p}_i, \mathbf{t}_i\}$ , but also the dependency of  $D_i$  on the measurements  $\{D_{i-1}, \dots, D_1\}$ . This dependency reflects the fact that the EM sensors are physically constrained at known locations along the catheter. It is thus expressed as the error in estimating the length along the B-spline curve between sensor  $D_i$  and all previous sensors  $\{D_{i-1}, \dots, D_1\}$ . Taking into account these considerations, we can write:

$$\begin{aligned} P(D_i|\zeta, D_1, \dots, D_{i-1}) &= \exp \left[ -\|\zeta(s_i) - \mathbf{p}_i\|^2 \right. \\ &\quad \left. - \left\| \frac{\zeta'(s_i)}{\|\zeta'(s_i)\|} - \mathbf{t}_i \right\|^2 \right. \\ &\quad \left. - \sum_{k=1}^i \left[ \int_{s_k}^{s_i} \|\zeta'(s)\| ds - L_{ik} \right]^2 \right] \end{aligned} \quad (12)$$

with  $s_i$  the curvilinear abscisse associated with EM sensor  $D_i$ , and  $L_{ik}$  the length between sensors  $D_i$  and  $D_k$  along the 3D curve described by  $\zeta$ .

The prior  $P(\zeta)$  in Eq. (10) represents the assumptions that (i) the catheter shape is a curve of minimum bending energy, and (ii) the catheter shape is described by a piece-wise cubic polynomial curve whose polynomial segments connect two successive EM sensors. These assumptions are necessary in order to reduce the solution space when trying to maximize Eq. (10).

Assumption (i) is introduced in the optimization problem by expressing the prior as

$$P(\zeta) = \exp \left[ - \int_0^L \|\zeta''(s)\|^2 ds \right] \quad (13)$$

with  $L$  the total length of the B-spline tube  $\zeta$ . Assumption (ii) is accounted for when optimizing Eq. (10) by directly fitting a piecewise cubic polynomial curve through the EM measurements. Instead of optimizing the knot points of the B-spline tube model  $\zeta$ , we optimize the coefficients of the cubic polynomial curves that connect the EM sensors. The knot points of the B-spline  $\zeta$  are then updated according to the result of this fitting.

Taking the logarithm of Eq. (10) and using Eqs. (11)–(13), the MAP problem for the 3D reconstruction consists in finding

$$\begin{aligned} \hat{\zeta} &= \arg \max_{\zeta} \sum_{i=1}^{n_s} \left[ -\|\zeta(s_i) - \mathbf{p}_i\|^2 - \left\| \frac{\zeta'(s_i)}{\|\zeta'(s_i)\|} - \mathbf{t}_i \right\|^2 \right. \\ &\quad \left. - \sum_{k=1}^i \left[ \int_{s_k}^{s_i} \|\zeta'(s)\| ds - L_{ik} \right]^2 \right] - \int_0^L \|\zeta''(s)\|^2 ds. \end{aligned} \quad (14)$$



This optimization is performed using a Levenberg–Marquardt optimization scheme. For simplicity, finite differences are used in the optimization procedure.

### 2.2.2. MLE for 2D tracking

The MLE is performed by registering the 3D tube model with its 2D projection in the fluoroscopic image. This registration uses the foreground/background model to segment out the catheter shape in the image plane by maximizing the likelihood  $P(\mathbf{x}|\zeta, \mathbf{y})$  with respect to the knot points of the B-spline. Assuming that pixels are independent and identically distributed, the likelihood function becomes:

$$P(\mathbf{x}|\zeta, \mathbf{y}) = \prod_{m=1}^{|\Omega|} P(\mathbf{x}_m|\zeta, \mathbf{y}_m). \quad (15)$$

In Eq. (15), the pixelwise likelihood functions  $P(\mathbf{x}_m|\zeta, \mathbf{y}_m)$  can be expressed as [21]:

$$\frac{P_f H_\epsilon(\Phi(\mathbf{x}_m)) + P_b(1 - H_\epsilon(\Phi(\mathbf{x}_m)))}{P_f \sum_{m=1}^{|\Omega|} H_\epsilon(\Phi(\mathbf{x}_m)) + P_b \sum_{m=1}^{|\Omega|} (1 - H_\epsilon(\Phi(\mathbf{x}_m)))}. \quad (16)$$

$P_f = P(\mathbf{y}_m|M_f)$  and  $P_b = P(\mathbf{y}_m|M_b)$  are the conditional probabilities of the measurements given the foreground and background models. The signed distance function  $\Phi(\mathbf{x})$  represents the projection contour  $\tau$  as a zero level-set ( $\Phi(\tau) = 0$ ) and  $H_\epsilon(x)$  is a smooth Heaviside function:

$$H_\epsilon(x) = \begin{cases} \frac{1}{2} \left( 1 + \frac{x}{\epsilon} + \frac{1}{\pi} \sin\left(\frac{x\pi}{\epsilon}\right) \right) & \text{if } -\epsilon \leq x \leq \epsilon, \\ 0 & \text{if } x < -\epsilon, \\ 1 & \text{if } x > \epsilon. \end{cases} \quad (17)$$

Taking the logarithm of both sides of Eq. (15), we find

$$\hat{\zeta} = \arg \max_{\zeta} \sum_{m=1}^{|\Omega|} \log P(\mathbf{x}_m|\zeta, \mathbf{y}_m) \quad (18)$$

by using a Levenberg–Marquardt optimization scheme. The interested reader is referred to Chang *et al.*'s work for more details on this MLE [21].

### 2.2.3. Optimization procedure

When solving the MAP problem (9), the posterior (10) is first maximized in 3D space only using EM data. This serves as an initial guess for the MLE (18) that is then performed. The MLE having registered the tube model in the image plane, the posterior (10) is again maximized, but only along the depth direction. The MLE and MAP estimations are then successively performed until convergence of the posterior  $P(\zeta|D, \Omega)$ . It is not guaranteed that this iterative approach will converge to the global

optimum. However, given good initial positions (e.g. knot points obtained through EM data), it will converge to a local optimum with useful values.

## 3. Evaluation of the Probabilistic Framework

The performance of the proposed probabilistic framework was assessed in a simulation environment and in a real-world experiment. In both setups, the shapes reconstructed using only EM sensors by maximizing Eq. (10) are compared with the shapes reconstructed with both EM sensors and fluoroscopic images and thus maximizing Eq. (9).

### 3.1. Simulation environment

A physics-based simulation environment has been developed to evaluate the performance of the proposed framework. This environment uses a minimum energy argumentation to simulate the insertion of an actuated catheter inside a virtual model of the vessel [24]. Such argumentation accounts for the complex catheter–vessel interaction and predicts the changes in the catheter shape resulting from specific positioning commands, such as insertion/retraction, rotation or bending of active segments. For every command that is sent to the simulation environment, the catheter bending energy and catheter–vessel interaction forces are estimated and used as inputs to iteratively compute the changes in the catheter shape that would minimize the energy of the entire system (catheter and vessel wall). This interaction model has been extensively validated for navigation of guidewires/catheters in endovascular surgery [24] and provides sufficiently realistic catheter shapes for the purpose of this study.

The vessel geometry for this simulation environment was extracted from patient CT scans provided by the University Hospital Leuven. Segmentation of the vessel of interest — the aorta — was carried out with the Mimics®Innovation Suite (Materialise, Leuven, Belgium). The simulated catheter is a 7Fr catheter with a bendable tip of 50 mm length. Predefined navigation commands were applied to the virtual catheter to steer it from the descending aorta to the aortic arch (83 mm insertion, tip bending of 40° and 70 mm insertion), cross the aortic arch and reach the aortic valve (tip bending of 50° and 175 mm insertion). These resulted in 337 simulation steps. For each of them, the simulation environment provided realistic catheter shapes, but also generated the corresponding synthetic fluoroscopic and EM sensor data.

Synthetic fluoroscopic images are generated from the CT scans that were used to create the virtual vessel model. A virtual camera simulates the fluoroscopic

system and allows viewing the CT volumetric data from different angles. Fluoroscopic images are generated from the camera point of view using a composite ray caster that simulates the X-ray physical attenuation process [25–27]. The 3D catheter shape generated by the simulator is then registered to the camera coordinate frame and projected onto the image plane to generate the 2D catheter shape in the fluoroscopic image. In the conducted simulation, the virtual camera was placed at 1200 mm from the patient, facing the natural plane of the aortic arch, with an image size of  $400 \times 600$ px, focal lengths of  $f_x = f_y = 2000$ px and a principal point placed at  $(200, 300)$ px.

Synthetic EM data are generated to simulate 5-DOFs EM sensors that are embedded at discrete positions along the catheter. The position and tangential orientation of these virtual sensors are directly calculated from the catheter shape that is generated from the simulation environment, taking into account the (fixed) distance between EM sensors. In the conducted simulation, five sensors are embedded within the virtual catheter. The most distal sensor is located at 10 mm from the catheter tip. The remaining ones are placed along the catheter, respectively, at 80, 80, 100 and 100 mm from the previous sensor. Note that the offset of the most distal sensor with respect to the catheter tip was introduced to mimic the sensor configuration of the catheter used during the real-world experiment and is accounted for when reconstructing the catheter shape.

Random noise is added to the position  $\mathbf{p}$  of the virtual EM sensors as follows:

$$\tilde{\mathbf{p}} = \mathbf{p} + \lambda \frac{\mathbf{d}}{\|\mathbf{d}\|} \quad (19)$$

with  $\mathbf{d} = [r_1 \ r_2 \ r_3]^T$ . Scalars  $r_{i=1,2,3} \in [-1, 1]$  are drawn from a random uniform distribution. The amplitude of the noise is determined by the value of  $\lambda$  that remains constant during the simulation. Random noise is also added to the tangent vector  $\mathbf{t}$  using random spherical coordinates:

$$\tilde{\mathbf{t}} = \text{rot}(\mathbf{a}, \psi; \mathbf{t}), \quad (20)$$

where  $\text{rot}(\mathbf{a}, \psi; \mathbf{t})$  rotates the vector  $\mathbf{t}$  with an angle  $\psi$  about the axis  $\mathbf{a} = [\cos \theta \sin \phi \ \sin \theta \sin \phi \ \cos \phi]^T$ . Angles  $\theta = \arccos(2r_4 - 1)$  and  $\phi = 2\pi r_5$  are generated with scalars  $r_{i=4,5} \in [0, 1]$  that are drawn from a random uniform distribution. The angle  $\psi$  is kept constant during the simulation. For both the sensor position  $\mathbf{p}$  and tangent  $\mathbf{t}$ , random uniform distributions for the noise direction and constant scalar values for the noise amplitude were chosen to simulate a worst-case scenario. The rationale is that the precision of the EM sensors is relatively high compared to their accuracy, the latter being affected by distortions of the EM field that are intrinsic to such tracking systems but that are also generated by external disturbances [12, 28]. As these

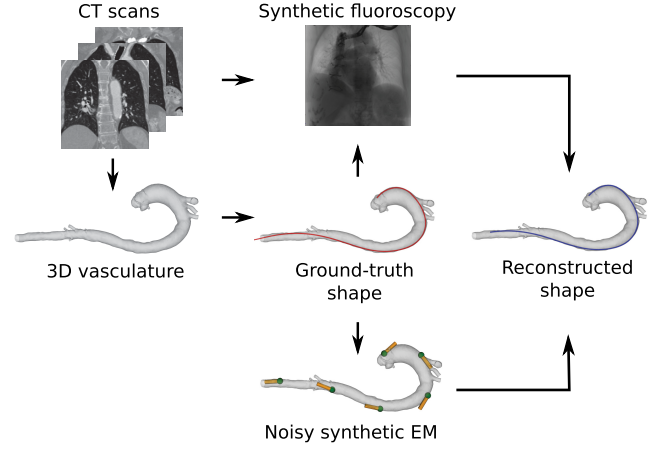


**Fig. 2.** Simulation environment. A catheterization is simulated in a virtual vessel, while corresponding synthetic fluoroscopic data and noisy EM measurements are generated. The generated measurements are used as inputs to reconstruct the catheter shape using the proposed probabilistic framework.

external disturbances can distort the EM field in numerous ways, we chose to represent their effect by attributing a random uniform distribution to the direction of the noise. The amplitude of the noise is then set to  $\lambda = 4$  mm and  $\psi = 3^\circ$  according to Lugez *et al.*'s study [12].

Within this environment, the virtual catheter shape is treated as a ground-truth, while the generated synthetic image and noisy EM data are used as input to reconstruct the catheter shape (Fig. 2). The reconstructed catheter shapes are then compared with the simulated shape using the metrics described in Sec. 3.3. Note that, in this simulation environment, registration errors between the EM tracking system and the fluoroscope are not simulated. The same applies for the registration errors of both measurement systems with respect to the preoperative mesh. The latter is important to account for to accurately localize the reconstructed catheter shape with respect to the patient anatomy, but this falls outside the scope of this paper. The interested reader is referred to, e.g., Sra and Ratnakumar's and Zhong *et al.*'s work for that matter [29, 30].

### 3.2. Experimental environment

Further evaluation has been conducted in a real-world experimental setup (Fig. 3). The setup was placed on top of a table-top NDI Aurora EM tracking system (Northern Digital Inc., Ontario, Canada). The catheter used during the experiment is a 7Fr TactiCath Quartz ablation catheter (St. Jude Medical, St. Paul, USA) in which four 5-DOFs EM sensors were embedded. The most distal sensor is located at 8 mm from the catheter tip. The remaining ones are placed along the catheter, respectively, at 86, 80, and 100 mm from the previous sensor.

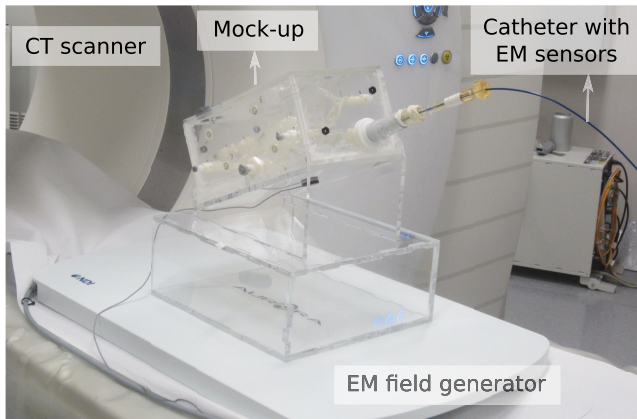


**Fig. 3.** Experimental setup. A catheter with EM sensors is inserted inside a 3D mock-up of the aorta. EM measurements and CT scans are acquired at different insertion positions.

During the experiment, the catheter was progressed and halted at five different locations along a 3D silicone mock-up of the aorta constructed based on patient data (Elastrat Sarl, Geneva, Switzerland). For each of these locations, the catheter was kept still, while EM measurements were recorded and a CT scan was acquired. The CT scans were processed with the Mimics®Innovation Suite (Materialise, Leuven, Belgium) to extract the ground-truth shapes of the catheter. They were also used to generate fluoroscopic views of the scene, as a fluoroscope was not available. The virtual camera simulating the fluoroscopic system was placed at 1200 mm from the mock-up, facing the natural plane of the aortic arch, with an image size of  $400 \times 600$ px, focal lengths  $f_x = f_y = 2900$ px and a principal point placed at (200,300)px. The EM data were registered to the CT data using conventional registration [31] with 13 markers. The mean registration error for these 13 markers was  $1.81 \pm 0.78$  mm and the maximum error, 3.64 mm. The acquired EM data and fluoroscopic views were then used to reconstruct the catheter shape using the proposed framework. The reconstructed shapes were compared to the ground-truth generated from the CT scans using the metrics described in Sec. 3.3.

### 3.3. Metrics for evaluation

Both in the simulation and experimental environments, the reconstructed shapes are quantitatively compared against the ground-truth shapes with the following metrics: the Hausdorff distance [32], the root mean square (RMS) error, and the RMS error along the respective  $x$ -,  $y$ - and  $z$ -coordinates of the fluoroscopic camera coordinate frame (the  $x$ - $y$  plane being the fluoroscopic plane). These metrics are computed for each step of the simulated catheterization and experimental insertion.

## 3.4. Results

The proposed shape reconstruction algorithm is implemented in C++. The computation time for optimizing a B-spline tube model comprising 20 knot points and 5 EM sensors is about 70 ms on a 2.90 GHz Intel Core i7 machine. Most of this time is spent computing the Frangi Filter magnitude for the image measurements  $y$  (50 ms). The MLE from Eq. (18) takes 12 ms, while solving the MAP of Eq. (14) requires 8 ms.

### 3.4.1. Simulation environment

Figure 4 shows the results of the shape reconstruction in the simulation environment for a few simulation steps. True (noise-free) EM measurements generated from the simulated ground-truth shape (black) are displayed as red spheres, while noisy EM measurements are in orange. Reconstructing the catheter shape using only the noisy EM data yields the shape in magenta. As can be seen in simulation step 90 in Fig. 4, the EM noise can be large enough to move the EM measurements — and thus the reconstructed shape — outside the vessel. By incorporating fluoroscopic measurements, the reconstructed shape is improved (green shape) and is now superimposed with the simulated ground-truth when looking at the fluoroscopic imaging plane.

The metrics described in Sec. 3.3 are computed for each of the 337 simulation steps, for both the reconstructed shape based on only EM data and the reconstructed shape based on EM and fluoroscopic data. These two sets (groups) of metrics are then compared using statistical hypothesis testing to find out whether the incorporation of fluoroscopy improves the reconstruction quality. Figure 5 shows the distribution of each metric for the 337 simulation steps, as well as the median and interquartile range (IQR) of the improvement factor (median | IQR). Q-Q plots and Shapiro-Wilk normality tests for each metric showed that the difference between groups is not normally distributed ( $p$ -value  $< 0.05$ ). Therefore, a Wilcoxon signed-rank test is performed to compare the two groups for each metric. The significance level is set to 0.05. A Bonferroni correction is applied to compensate for repeated testing. An effect size [33] defined as the matched-pairs rank-biserial correlation [34] is also computed for each metric. This effect size ranges from  $-1$  to  $1$ . It is positive (favorable effect) when incorporating fluoroscopic data improves the reconstruction quality (decreases the reconstruction error). The larger the absolute value of the effect size, the more pronounced the effect is.

The results of this statistical analysis (Table 1) suggest that the reconstruction quality significantly improves when incorporating the fluoroscopic data into the shape reconstruction procedure: for the Hausdorff

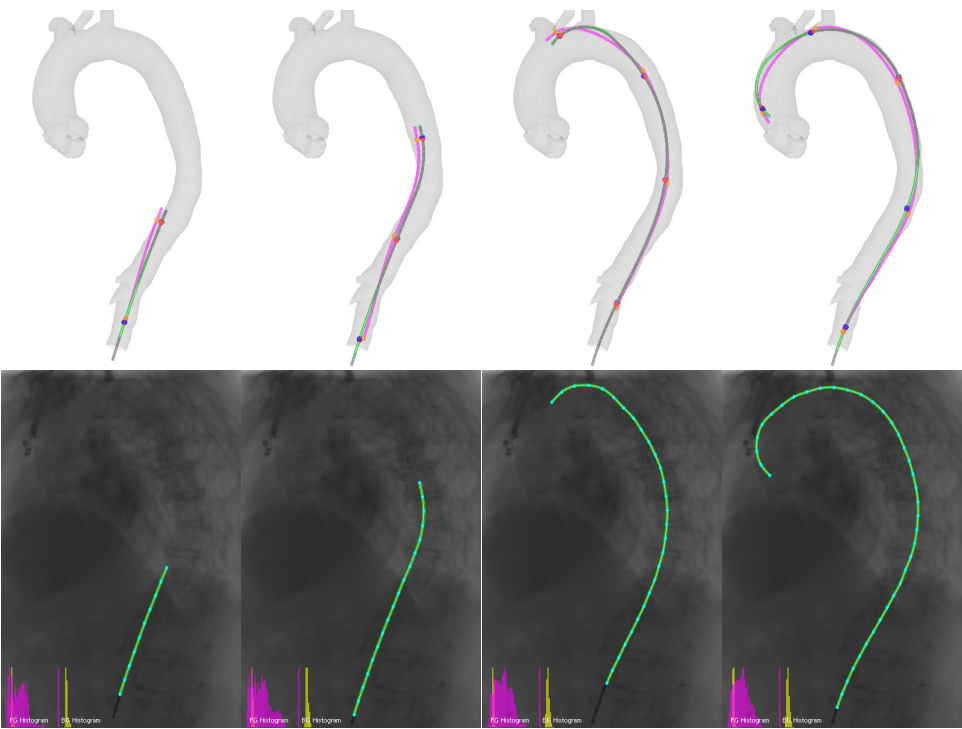


**Fig. 4.** Simulation environment for evaluating the shape reconstruction algorithm. From left to right: simulation steps 90, 170, 317 and 397. Top row: 3D view of the simulated catheterization from the point of view of the virtual camera simulating the fluoroscope, displaying the ground-truth catheter shape (black) and EM sensors (red spheres), the simulated noisy EM sensors (orange spheres), the reconstructed shape using only EM data (magenta), the reconstructed shape using EM and fluoroscopic data (green — here superimposed with the ground-truth), and the estimated position of the EM sensors after reconstruction (blue spheres, here superimposed with the simulated ground-truth EM sensors). Bottom row: fluoroscopic view with the simulated ground-truth shape (black) and the projection of the catheter shape reconstructed using EM and fluoroscopic data (green — here superimposed with the simulated ground-truth).

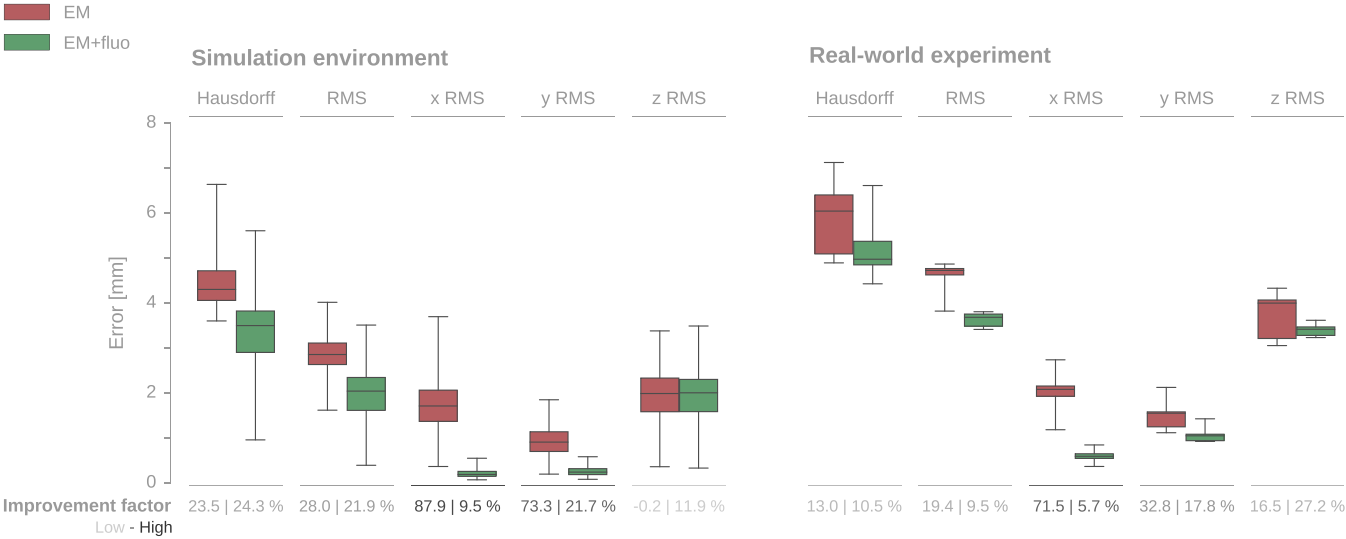


**Fig. 5.** Error distribution when using only EM data (red) and using both EM and fluoroscopic data (green) in the simulation environment (left) and in the real-world experimental setup (right). The whiskers of the boxplot indicate the minimum and maximum values of the errors. The median and IQR of the improvement factor due to the incorporation of fluoroscopic data is presented in percentage for each metric and is labeled (median | IQR). Most of the improvement occurs in the  $x$ - $y$  plane, which corresponds to the fluoroscopic plane.



and RMS errors, the  $p$ -value of the Wilcoxon signed-rank test is  $p_W \ll 0.05$  and the effect size is  $ES \approx 1$ . As expected, the reconstruction accuracy mostly improves in the plane of the fluoroscopic image ( $p_W \ll 0.05$ ,  $ES \approx 1$ ) and has little to no effect along the depth direction ( $p_W \gg 0.05$ ,  $ES \approx 0$ ).

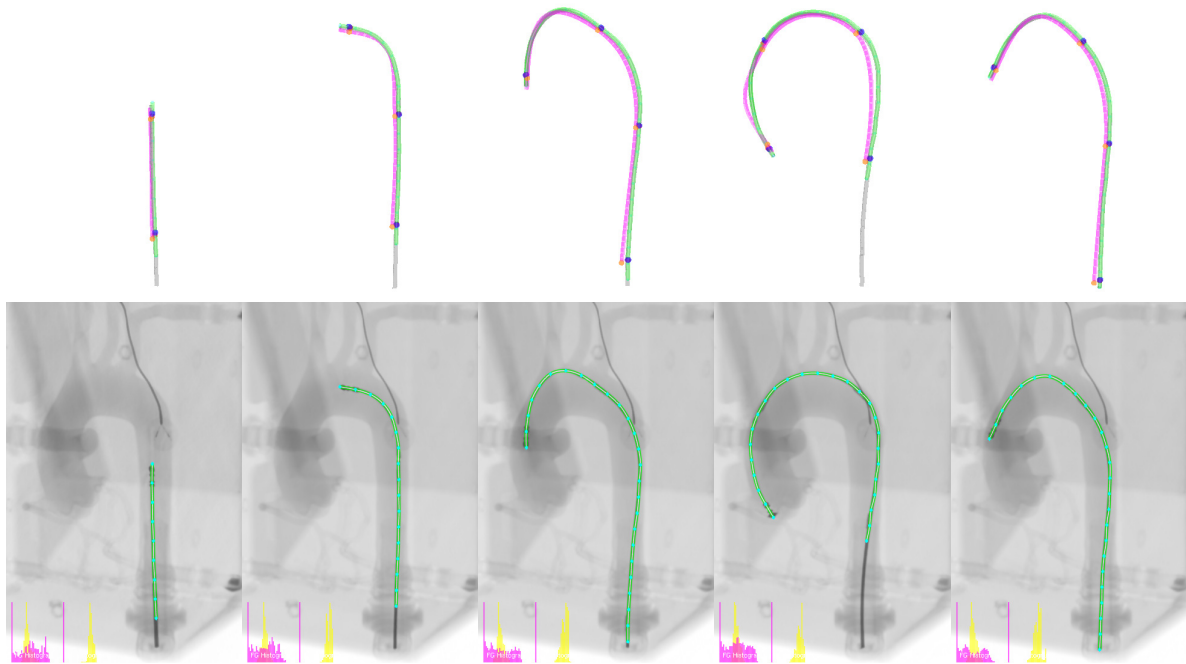
### 3.4.2. Experimental setup

Figure 6 shows the results of the shape reconstruction in the real-world experimental setup for the five positions of the catheter inside the mock-up. As for the simulation environment, the shape reconstructed based only on EM data (magenta) is shifted with respect to the simulated ground-truth (black shape). The incorporation of fluoroscopic measurements improves the reconstructed shape (green) that is now superimposed with the ground-truth when looking at the imaging plane.

As with the simulation environment, the metrics described in Sec. 3.3 are computed for the five insertion steps. Figure 5 shows the distribution of each metric, as well as the median and IQR of the improvement factor. Although less pronounced than in the simulation environment, a similar trend is observed, namely an

improvement in the reconstruction quality that mainly occurs in the fluoroscopic plane. To further confirm this trend, the reconstruction errors of the two groups (EM and EM+fluo) are compared using statistical hypothesis testing. As the sample size (number of insertion steps) is small, a non-normal distribution for the difference between the two groups is assumed. To compare each metric between the two groups, a Wilcoxon signed-rank test with a significance level of 0.05 and a Bonferroni correction is performed. The matched-pairs rank-biserial correlation [34] is computed as an effect size.

The results in Table 1 do not yield the conclusion that incorporating fluoroscopic information significantly changes the reconstruction errors ( $p_W > 0.05$ ). These results are not in line with what is expected, but could be explained by the low power of statistical testing when dealing with small sample sizes [35]. Although the large effect sizes (Hausdorff  $ES = 0.87$ , RMS and  $x$  and  $y$  RMS  $ES = 1$ ) suggest there could be a difference in reconstruction, we cannot rule out that this is due to random effects. Further investigation with the aim of increasing the power of the statistical analysis is thus necessary to statistically confirm the trend that incorporating fluoroscopic data improves the reconstruction quality.



**Fig. 6.** Experimental evaluation of the shape reconstruction algorithm for five insertion positions within the mock-up. Top row: 3D view of the insertion from the point of view of the virtual camera simulating the fluoroscope, displaying the ground-truth catheter shape (black) and EM sensors (red spheres), the simulated noisy EM sensors (orange spheres), the reconstructed shape using only EM data (magenta), the reconstructed shape using EM and fluoroscopic data (green, here superimposed with the ground-truth), and the estimated true position of the EM sensors (blue spheres, here superimposed with the simulated ground-truth EM sensors). Bottom row: fluoroscopic view with the ground-truth shape (black) and the projection of the catheter shape reconstructed using EM and fluoroscopic data (green, here superimposed with the ground-truth).

**Table 1.** Summary of the statistical analysis comparing the reconstruction errors when using only EM data (EM) and using both EM and fluoroscopic data (EM+fluo) in the simulation environment (left) and in the real-world experimental setup (right): median and IQR (median | IQR) of the reconstruction errors [mm] of both groups; improvement factor (IF) [%] due to the incorporation of fluoroscopic data;  $p$ -value of the Wilcoxon signed-rank test ( $p_W$ ) to differentiate both groups and effect size of incorporating fluoroscopic data (ES).

		EM	EM+fluo	IF	$p_W$	ES			EM	EM+fluo	IF	$p_W$	ES
Simulation	Hausdorff	4.3   0.7	3.5   0.9	23.5   24.3	$< 10^{-50}$	0.97	Experiment	Hausdorff	6.0   1.3	4.9   0.5	13.0   10.5	0.62	0.87
	RMS	2.8   0.5	2.0   0.7	28.0   21.9	$< 10^{-50}$	0.99		RMS	4.7   0.1	3.7   0.3	19.4   9.5	0.31	1
	x RMS	1.7   0.7	0.2   0.1	87.9   9.5	$< 10^{-50}$	1		x RMS	2.1   0.2	0.6   0.1	71.5   5.7	0.31	1
	y RMS	0.9   0.4	0.2   0.1	73.3   21.7	$< 10^{-50}$	0.99		y RMS	1.6   0.3	1.0   0.1	32.9   17.8	0.31	1
	z RMS	2.0   0.7	2.0   0.7	-0.2   11.9	1	-0.03		z RMS	4.0   0.9	3.4   0.2	16.5   27.2	1	0.6

#### 4. Conclusion

A probabilistic framework has been proposed to incorporate the 2D dense information extracted from fluoroscopic images into the 3D catheter shape estimate obtained from EM sensor data. The proposed method models the catheter as a B-spline tube and solves the overall MAP problem as a succession of MLE in the image plane and MAP problem in 3D space until convergence. Experiments in a simulation environment and in a real-world setup showed the feasibility of reconstructing the catheter shape using only EM sensors and using both EM and fluoroscopic measurements. The reconstruction accuracy in the simulation environment and in the real-world setup shows a tendency to improve when including fluoroscopic data. Although statistically significant in the simulation environment, this improvement does not seem to be statistically significant in the real-world experiment, which could be due to the low power of the statistical testing. Such results are nevertheless promising, as the use of fluoroscopy could be limited to risk-prone areas, thus leading to less invasive interventions with potentially improved decision making and catheter steering during surgery.

Future work will focus on improving the power of the statistical analysis in the real-world experiment by, e.g. increasing the number of samples. The influence of the measurement noise will also be further investigated by improving the noise model of the EM sensors in the simulation environment, as well as incorporating noise and distortion in the fluoroscopic images and registration errors between the EM data and fluoroscopic images. As the proposed approach is not guaranteed to converge towards a global optimum, future work will also attempt to increase the robustness of the overall framework and achieve a higher reconstruction accuracy by incorporating learning-based measurements [6] or relevant prior information, e.g. using temporal tracking or predictive mechanical models of robotic catheters.

#### Acknowledgments

Research funded by the European Commission's 7th Framework Programme FP7-ICT - Under grant agreement No. 601021, EU project CASCADE.

#### References

1. Y. Kassahun, B. Yu, A. T. Tibebe, D. Stoyanov, S. Giannarou, J. H. Metzen and E. Vander Poorten, Surgical robotics beyond enhanced dexterity instrumentation: A survey of machine learning techniques and their role in intelligent and autonomous surgical actions, *Int. J. Comput. Assist. Radiol. Surg.* **11**(4) (2016) 553–568. DOI: 10.1007/s11548-015-1305-z
2. A. Vahanian, O. R. Alfieri, N. Al-Attar, M. J. Antunes, J. Bax, B. Cormier, A. Cribier, P. De Jaegere, G. Fournial, A. P. Kappetein *et al.*, Transcatheter valve implantation for patients with aortic stenosis: A position statement from the european association of cardiothoracic surgery (eacts) and the european society of cardiology (esc), in collaboration with the european association of percu, *Eur. Heart J.* **29**(11) (2008) 1–8.
3. A. Rolls, C. Riga, C. Bicknell, D. Stoyanov, C. Shah, I. Van Herzele, M. Hamady and N. Cheshire, A pilot study of video-motion analysis in endovascular surgery: Development of real-time discriminatory skill metrics, *Eur. J. Vasc. Endovasc. Surg* **45**(5) (2013) 509–515.
4. C. Tercero, S. Ikeda, T. Uchiyama, T. Fukuda, F. Arai, Y. Okada, Y. Ono, R. Hattori, T. Yamamoto, M. Negoro and I. Takahashi, Autonomous catheter insertion system using magnetic motion capture sensor for endovascular surgery, *Int. J. Med. Robot.* **3** (2007) 52–58.
5. M. C. Yip and D. B. Camarillo, Model-less feedback control of continuum manipulators in constrained environments, *IEEE Trans. Robot.* **30**(4) (2014) 880–889.
6. P. Wang, T. Chen, Y. Zhu, W. Zhang, S. K. Zhou and D. Comaniciu, Robust guidewire tracking in fluoro-scopy, *IEEE Conf. Computer Vision and Pattern Recognition (CVPR)* (2009), pp. 691–698.
7. H. Heibel, B. Glocker, M. Groher, M. Pfister and N. Navab, Interventional tool tracking using discrete optimization, *IEEE Trans. Med. Imag.* **32**(3) (2013) 544–555.
8. M. Schenderlein, S. Stierlin, R. Mancke, V. Rasche and K. Dietmayer, Catheter tracking in asynchronous biplane fluoroscopy images by 3D B-snakes, in *Imaging* Vol. 7625 (2010), pp. 76251U–76251U–9.
9. A. M. Franz, T. Haidegger, W. Birkfellner, K. Cleary *et al.*, Electromagnetic tracking in medicine - A review of technology, validation, and applications, *IEEE Trans. Med. Imag.* **33**(8) (2014) 1702–1725.

10. R. Chan, R. Manzke, A. Popovic, G.W. 'T Hooft, H. Von Busch, Optical shape sensing fiber for tip and shape characterization of medical instruments, WO Patent App. PCT/IB2012/050,339 (2012). <https://patentscope.wipo.int/search/en/detail.jsf?docId=W02012101584>
11. S. L. Lee, C. Riga, L. Crowie, M. Hamady, N. Cheshire and G. Z. Yang, An instantiability index for intra-operative tracking of 3D anatomy and interventional devices, *Medical Image Computing and Computer-Assisted Intervention — MICCAI 2011*, Lecture Notes in Computer Science, Vol. 6891 (Springer, Berlin, Heidelberg, 2011), pp. 49–56. DOI: 10.1007/978-3-642-23623-5.7.
12. E. Lugez, H. Sadjadi, D. R. Pichora, R. E. Ellis, S. G. Akl and G. Fichtinger, Electromagnetic tracking in surgical and interventional environments: Usability study, *Int. J. Comput. Assist. Radiol. Surg.* **10**(3) (2015) 253–262. DOI: 10.1007/s11548-014-1110-0.
13. M. Azizian and R. Patel, Data fusion for catheter tracking using Kalman filtering: Applications in robot-assisted catheter insertion, in *SPIE Medical Imaging*, Vol. 7964, No. 519 (2011), pp. 796413–796413–11.
14. S. Tully, G. Kantor, M. A. Zenati and H. Choset, Shape estimation for image-guided surgery with a highly articulated snake robot, in *2011 IEEE/RSJ Int. Conf. Intelligent Robots and Systems (IEEE)*, September 2011, pp. 1353–1358.
15. A. Dore, G. Smoljkic, E. Vander Poorten, M. Sette, J. Vander Sloten and G.-Z. Yang, Catheter navigation based on probabilistic fusion of electromagnetic tracking and physically-based simulation, in *2012 IEEE/RSJ Int. Conf. Intelligent Robots and Systems (IEEE)*, October 2012, pp. 3806–3811.
16. A. Vandini, C. Bergeles, F.-y. Lin and G.-z. Yang, Vision-based intraoperative shape sensing of concentric tube robots, *Int. Conf. Intelligent Robots and Systems - IROS*, Hamburg (2015), pp. 2603–2610.
17. S. C. Ryu and P. E. Dupont, FBG-based shape sensing tubes for continuum robots, in *2014 IEEE Int. Conf. Robotics and Automation (ICRA)* (IEEE), May 2014, pp. 3531–3537.
18. R. J. Roesthuis, S. Janssen and S. Misra, On using an array of fiber Bragg grating sensors for closed-loop control of flexible minimally invasive surgical instruments, in *2013 IEEE/RSJ Int. Conf. Intelligent Robots and Systems (IEEE)*, November 2013, pp. 2545–2551.
19. C. Ledermann, J. Mintenbeck, Y. Ding, H. Pauer and H. Wörn, Closed-loop control of a flexible instrument using an integrated FBG-based shape sensor, *Int. Conf. Advanced Technology & Sciences (ICAT'15)*, August 2015, Antalya, Turkey, pp. 67–72.
20. C. Ledermann, H. Pauer and H. Woern, Fiber optical sensor system for shape and haptics for flexible instruments in minimally invasive surgery: Overview and status quo, in *Proc. SPIE*, eds. J. M. López-Higuera, J. D. C. Jones, M. López-Amo and J. L. Santos, Vol. 9157, 2014, p. 915766.
21. P.-I. Chang, A. Rolls, H. D. Praetere, E. V. Poorten, C. V. Riga, C. D. Bicknell and D. Stoyanov, Robust catheter and guidewire tracking using B-spline tube model and pixel-wise posteriors, *IEEE Robot. Autom. Lett.* **1**(1) (2016) 303–308.
22. M. G. Cox, The numerical evaluation of B-splines, *IMA J. Appl. Math.* **10**(2) (1972) 134–149.
23. K. Qin, General matrix representations for b-splines, *Vis. Comput.* **16**(3) (2000) 177–186.
24. T. Alderliesten, M. K. Konings and W. J. Niessen, Modeling friction, intrinsic curvature, and rotation of guide wires for simulation of minimally invasive vascular interventions, *IEEE Trans. Biomed. Eng.* **54**(1) (2007) 29–38.
25. M. Muniyandi, S. Cotin, M. Srinivasan and S. Dawson, Real-time PC based X-ray simulation for interventional radiology training, in *Studies in Health Technology and Informatics*, Vol. 94 (IOS Press Ebooks, 2003), pp. 233–239. DOI: 10.3233/978-1-60750-938-7-233.
26. Y. Otake, M. Armand, R. S. Armiger, M. D. Kutzer, E. Basafa, P. Kazanzides and R. H. Taylor, Intraoperative image-based multiview 2D/3D registration for image-guided orthopaedic surgery: Incorporation of fiducial-based C-Arm tracking and GPU-acceleration, *IEEE Trans. Med. Imag.* **31**(4) (2012) 948–962.
27. T. Heimann, P. Mountney, M. John and R. Ionasec, Real-time ultrasound transducer localization in fluoroscopy images by transfer learning from synthetic training data, *Med. Image Anal.* **18**(8) (2014) 1320–1328.
28. C. Nafis, V. Jensen and R. von Jako, Method for evaluating compatibility of commercial Electromagnetic (EM) micro sensor tracking systems with surgical and imaging tables, in *Proc. SPIE 6918, Medical Imaging 2008: Visualization, Image-guided Procedures, and Modeling*, Vol. 6918 (2008), pp. 691820–691835, DOI: 10.1117/12.769513.
29. J. Sra and S. Ratnakumar, Cardiac image registration of the left atrium and pulmonary veins, *Heart Rhythm* **5**(4) (2008) 609–617.
30. H. Zhong, T. Kanade and D. Schwartzman, Virtual touch: An efficient registration method for catheter navigation in left atrium, *Med. Image Comput. Comput.-Assist. Interv.* **9**(Pt 1) (2006) 437–444.
31. C. W. C. Spoor and F. E. Veldpaus, Rigid body motion calculated from spatial co-ordinates of markers, *J. Biomech.* **13** (1980) 391–393.
32. R. Veltkamp, Shape matching: Similarity measures and algorithms, in *Proc. Int. Conf. Shape Modeling and Applications* (IEEE Computer Society, 2001), pp. 188–197.
33. G. M. Sullivan and R. Feinn, Using effect size or why the p value is not enough, *J. Graduate Med. Edu.* **4**(3) (2012) 279–282.
34. D. S. Kerby, The simple difference formula: An approach to teaching nonparametric correlation, *Comprehensive Psychol.* **3** (2014) 11.IT.3.1.
35. J. Cohen, *Statistical Power Analysis for the Behavioral Sciences*, 2nd edn. (Lawrence Erlbaum Associates, Publishers, 1988).



**Phuong Toan Tran** received the M.Sc. degree in Biomedical Engineering from the Université Libre de Bruxelles, Brussels, Belgium, in 2012. He currently is a Ph.D. researcher within the Robot Assisted Surgery group at the Mechanical Engineering Department of KU Leuven, Belgium. His research interests include sensing, control and virtual reality simulation of continuum robots for minimally invasive surgical applications.



**Ping-Lin Chang** received a B.S. degree from the Department of Engineering Science at the National Cheng Kung University in Taiwan in 2007, and graduated from Electronics and Computer Science at the University of Southampton in the United Kingdom, with a M.Sc. degree in artificial intelligence in 2010. He was awarded a Ph.D. degree under the supervision of Dr. Eddie Edward and Prof. Andrew Davison at the Department of Computing at Imperial College London in 2015. He afterward worked at the Surgical Robot Vision Group at the Centre for Medical Image Computing (CMIC) and Department of Computer Science, University College London (UCL), under the supervision of Dr. Danail Stoyanov. He particularly focuses on research topics in computer vision and machine learning.





**Herbert De Praetere** received his bachelor and master degree from KU Leuven, Belgium in 2000 and 2004, respectively. He obtained his degree of general surgeon in 2010 and finished his further specialization of cardiac surgery in 2012. In 2012, he started his Ph.D. titled: "The influence of minimal access surgery on biological outcome: in search of involved pathophysiological pathways." Since 2012 he was working as a staff member in the university hospital of Leuven. Since 2015 he is working also in the general hospital of Bonheiden as a cardiac surgeon. In both hospitals he takes a special interest in minimal invasive techniques, especially transcatheter valves and robotic enhanced techniques.



**Julie Maes** received her B.S. in Mechanical Engineering and M.S. degree in Biomedical Engineering from the University of Leuven, in 2012 and 2014, respectively. In 2014, she joined the Medical department of Materialise as an application engineer for cardiovascular applications. Today she is a product engineer for cardiovascular applications at Materialise Medical. Her current position includes responsibilities in cardiovascular applications of the Mimics software and the HeartPrint and HeartPrint Research products.



**Dominiek Reynaerts** obtained an M.S. degree (1986) and a Ph.D. degree (1995) in Mechanical Engineering from KU Leuven. He is a Full Professor in micro- and precision engineering at the KU Leuven, Department of Mechanical Engineering and he is since 2008 also chairing this department with a total staff of about 320 people. His major research interests include manufacturing and machine design with focus on precision engineering and micromechanical actuation systems, with main applications in medical robotics and instrumentation, machine tools and metrology, and energy systems. He is member of IEEE, EUSPEN — European Society of Precision Engineering and Nanotechnology — and of EFFRA — European Factories of the Future Research Association.



**Jos Vander Sloten** obtained his M.S. and Ph.D. in Mechanical Engineering from KU Leuven in 1985 and 1990, respectively. Currently he is a Full Professor at the Biomechanics Section, Department of Mechanical Engineering at KU Leuven. He also chairs the Leuven Medical Technology Centre (L-MTC). His teaching assignments are engineering mechanics, problem solving and engineering design, computer integrated surgery systems. His research interests are computer applications in musculoskeletal biomechanics and computer integrated surgery, on which he authored more than 160 journal papers. He is member of the council of the Belgian Society for Medical and Biological Engineering and Computing, and a former council member of the European Society of Biomechanics. In the European Alliance for Medical and Biological Engineering and Science (EAMBES) he served as secretary-general (2003–2004), president-elect (2005) and president (2006). He was elected Founding Fellow of EAMBES. He is a co-founder of the spin-off company Custom8, member of the board of directors of the company Materialise NV and provides consultancy to the company Mobelife NV.



**Danail Stoyanov** received the Ph.D. degree in medical image computing from Imperial College London. He is currently an Associate Professor at the Centre for Medical Image Computing and the Department of Computer Science, University College London, where he leads the Surgical Robot Vision Research Group and is Director of the UCL Robotics Institute. His research interests are in minimally invasive and robotic assisted surgery, surgical navigation and guidance, surgical imaging and workflow analysis. He is General Chair for the International Conference on Information Processing in Computer Assisted Interventions, a deputy editor for the International Journal of Computer Assisted Radiology and Surgery and an associate editor for the IEEE Robotics and Automation Letters.



**Emmanuel Vander Poorten** received his B.S. and M.S. degree from the University of Leuven, Belgium and his Ph.D. degree from the University of Kyoto, Japan, all in Mechanical Engineering in 1998, 2000 and 2007, respectively. From 2007 to 2014, he was a Postdoctoral Researcher at the University of Leuven, Belgium. From 2015, he joined the faculty at the Department of Mechanical Engineering, Belgium, where he is now an Assistant Professor. His research interests include design and control of

haptic interfaces, surgical robots, surgical instruments and surgery training systems.